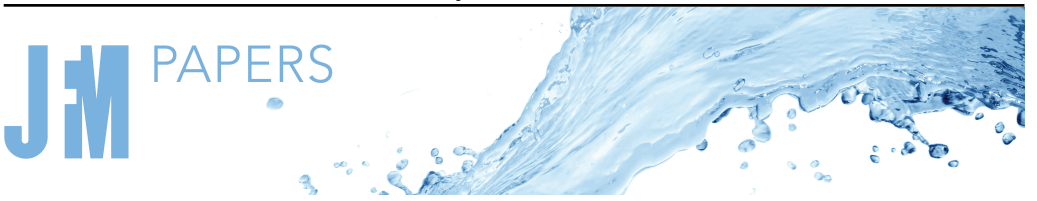
J. Fluid Mech. (2026), *vol.* 1032, A5, doi:10.1017/jfm.2026.11312



Nonlinear subcritical free-surface flow past topography: exponential-asymptotics solution

Takeshi Kataoka[1] **and T.R. Akylas**[2]

[1]Department of Mechanical Engineering, Kobe University, 1-1 Rokkodai, Nada, Kobe 657-8501, Japan

[2]Department of Mechanical Engineering, Massachusetts Institute of Technology, Cambridge, MA 02139, USA

Corresponding author: T.R. Akylas, trakylas@mit.edu

(Received 24 October 2025; revised 22 January 2026; accepted 8 February 2026)

A theoretical study is made of steady, subcritical (Froude number $F < 1$) two-dimensional free-surface flow due to a uniform stream flowing over smooth, locally confined bottom topography of large horizontal extent ($L \gg 1$) and finite peak height ($\varepsilon = O(1)$). In earlier work, this flow was analysed based on the nonlinear shallow-water equations which neglect the effects of dispersion altogether. This so-called hydraulic theory predicts a steady disturbance confined in the vicinity of the topography if ε is below a critical value $\varepsilon_{crit}(F)$. The present asymptotic analysis of the full potential flow equations focuses on how dispersive effects (controlled by $\mu = 1/L \ll 1$) influence this steady state, particularly in regard to a steady short-scale radiating wave downstream that is ignored by hydraulic theory. Utilizing exponential asymptotics, it is shown that as ε is increased this dispersive wave, whose amplitude is formally exponentially small with respect to μ, grows sharply and ultimately it becomes comparable with the hydraulic wave disturbance when ε approaches ε_{crit}. Thus, the nonlinear shallow-water equations break down in the vicinity of ε_{crit} regardless of $\mu \ll 1$. The asymptotic results are supported by numerical solutions of the full potential flow theory, which also reveal a limiting ε, $\varepsilon_{lim} \approx \varepsilon_{crit}$, above which steady wave responses cannot be computed. For ε just below ε_{lim}, the downstream wave resembles a steep steady Stokes periodic wave, while for ε slightly above ε_{lim} unsteady computations suggest that the downstream disturbance steepens and breaks.

Key words: waves/free-surface flows, surface gravity waves, wave breaking

1. Introduction

This paper revisits two-dimensional free-surface flow due to a uniform stream U_* flowing over smooth, locally confined (width L_* in the streamwise direction) topography of peak height h_* (figure 1). Ignoring viscosity and surface tension, the flow is controlled by the

© The Author(s), 2026. Published by Cambridge University Press.

https://doi.org/10.1017/jfm.2026.11312 Published online by Cambridge University Press

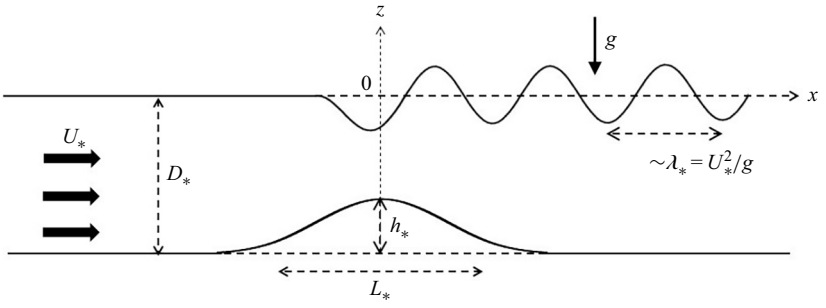


Figure 1. Flow schematic.

dimensionless parameters

$$\mu = \frac{\lambda_*}{L_*}, \qquad \varepsilon = \frac{h_*}{\lambda_*}, \qquad D = \frac{D_*}{\lambda_*}, \tag{1.1}$$

where $\lambda_* = U_*^2/g$ is the gravity wavescale (g is the gravitational acceleration) and D_* is the (constant) undisturbed water depth far upstream. The depth parameter D also specifies the Froude number

$$F = \frac{U_*}{(gD_*)^{1/2}} = \frac{1}{D^{1/2}}. \tag{1.2}$$

Using potential flow theory, the classical analytical treatment (e.g. Stoker 1957) assumes that the topography has infinitesimal height ($\varepsilon \to 0$). The boundary conditions on the free surface and the topography then are linearized about the undisturbed stream over a flat bottom and the problem is solved by transforms. This linear solution approaches a steady state that features a radiating gravity wave train downstream if the flow is subcritical ($F < 1$) but remains localized over the topography if the flow is supercritical ($F > 1$). At $F = 1$, the linear steady-state response breaks down due to a resonance phenomenon. As a result, for $F \approx 1$ nonlinearity cannot be neglected, and the response exhibits periodic shedding of solitary waves upstream (Akylas 1984; Cole 1985).

A complementary theoretical approach is based on the nonlinear shallow-water equations, which formally approximate the full potential flow equations in the limit $\mu \to 0$ with $\varepsilon = O(1)$. This so-called 'hydraulic' theory is expected to be valid for topography of large horizontal extent and finite height. Due to the assumption $\mu \to 0$, the hydraulic approximation neglects dispersion altogether and cannot account for steady radiating waves. On the other hand, it has been used to study the formation of hydraulic jumps and related phenomena due to finite-height topography, which are beyond the reach of linear theory (see Baines (1995) for a comprehensive review).

The focus here is on steady, subcritical flow over extended, finite-height topography

$$F < 1 \ \ (D > 1), \qquad \mu \ll 1, \qquad \varepsilon = O(1). \tag{1.3}$$

For $F < 1$, the nonlinear shallow-water theory predicts a steady state only if the topography peak height is below a critical value, $\varepsilon < \varepsilon_{crit}(F)$. The associated free-surface disturbance is localized in the vicinity of the topography. When $\varepsilon > \varepsilon_{crit}$, the flow is partially blocked by the topography and hydraulic jumps form upstream and downstream (Long 1954; Houghton & Kasahara 1968). These two types of hydraulic states also were confirmed by laboratory experiments (Long 1954, 1970).

https://doi.org/10.1017/jfm.2026.11312 Published online by Cambridge University Press

In recent related theoretical work, (Kataoka & Akylas (2024), hereafter referred to as KA2024) studied asymptotically the effects of small dispersion ($0 < \mu \ll 1$) on steady subcritical free-surface flow ($F < 1$) over smooth topography of small but finite height ($0 < \varepsilon \ll 1$). As noted above, when $F < 1$, dispersion is responsible for the appearance of a steady radiating gravity wave train downstream. Remarkably, in the weakly nonlinear–weakly dispersive limit, $\mu, \varepsilon \ll 1$, the amplitude of this wave, although formally exponentially small with respect to μ, hinges on a nonlinear mechanism. Furthermore, comparisons of asymptotic results with numerical solutions of the full water-wave equations suggest that this mechanism controls the wave response for a broad range of flow conditions, in sharp contrast to the classical linear theory which has very limited validity.

In light of these findings, it is natural to wonder about the effects of weak dispersion ($0 < \mu \ll 1$) in the nonlinear locally confined steady state predicted by hydraulic theory for subcritical flow ($F < 1$) over topography of finite $\varepsilon < \varepsilon_{crit}(F)$. This issue is addressed here by developing an asymptotic theory in the limit $\mu \ll 1$ for the downstream wave response due to smooth, symmetric topography of $O(1)$ height. Similar to KA2024, the wave amplitude R is exponentially small with respect to μ, $R = O(\exp(-q/\mu))$. However, rather than a constant set by the linear solution, here the (positive) exponent q is found to be a decreasing function of ε with $q \to 0$ as $\varepsilon \to \varepsilon_{crit}$. Thus, increasing the topography height boosts the radiating wave. Moreover, for ε near the critical topography height ε_{crit}, this (formally exponentially small) wave approaches the same level as the hydraulic disturbance over the topography. As a result, the nonlinear shallow-water equations are expected to break down in the vicinity of ε_{crit}, however small μ may be.

The asymptotic results for the radiating wave amplitude and phase are confirmed by numerical solutions of the full steady water-wave equations for topography with a sech profile. These computations also indicate the existence of a limiting topography height, ε_{lim}, close to ε_{crit} depending on F and μ, above which a steady solution that approaches the uniform stream far upstream and remains finite downstream, is not possible. For ε just below ε_{lim}, the computed downstream steady wave resembles a steep Stokes wave. In addition, when ε is slightly above ε_{lim}, unsteady computations suggest that the disturbance downstream of the topography steepens and breaks.

Theoretically, in the limit $\mu \ll 1$, the radiating wave downstream cannot be captured by perturbation expansions in powers of μ, as the wave amplitude is exponentially small with respect to μ. Furthermore, as the wavelength is not long compared with the water depth, this wave cannot be computed based on approximate nonlinear long-wave theories, such as the Serre–Green–Naghdi equations (Liapidevskii & Gavrilova 2008). Accordingly, the present analysis deals with the full water-wave equations and makes use of exponential (beyond-all-orders) asymptotics. The appropriate techniques were developed recently in the context of a simple model problem (Kataoka & Akylas (2025), hereafter referred to as KA2025). Here, in the interest of brevity, we outline the main steps of the asymptotic analysis, and further mathematical details can be found in KA2025.

Earlier exponential-asymptotics treatments of nonlinear free-surface flow past topography (e.g. Lustri, McCue & Binder (2012) and references given therein) assumed $F \ll 1$ and general – not necessarily locally confined and smooth – topography profile (e.g. a step) with peak height comparable to the water depth, $h_*/D_* = O(1)$. In this limit, it follows from (1.2) that the topography is submerged at a large depth relative to the gravity wavescale λ_*, which explains why the disturbance at the free surface is exponentially small with respect to F. By contrast, in the flow regime (1.3) of interest here, $F = O(1)$ so the topography is submerged at a depth comparable to λ_*, but $\mu \ll 1$ implies that λ_* is much shorter than the topography width L_*. Owing to this scale separation and the assumption

https://doi.org/10.1017/jfm.2026.11312 Published online by Cambridge University Press

that the topography profile $h(x)$ is locally confined and smooth (such that its Fourier transform decays exponentially at large wavenumber), the radiating wave has exponentially small amplitude with respect to μ. In addition, a notable difference from previous work is that here the radiating wave amplitude approaches $O(1)$ close to the critical topography height ε_{crit}, however small μ may be.

2. Preliminaries

We shall work with dimensionless variables throughout, using L_* as reference length scale in the streamwise (x) direction and $\lambda_* = U_*^2/g$ in the vertical (z) direction (figure 1). The steady flow of interest occupies the region $(-\infty < x < \infty, -D + \varepsilon h < z < \eta)$, where $z = \eta(x)$ denotes the free-surface elevation (scaled with λ_*) and $h(x)$ the topography profile (scaled with the peak height h_*).

2.1. *Formulation in the physical domain*

Assuming potential flow, the perturbation velocity potential $\varphi(x, z)$ (scaled with U_*L_*) from the uniform stream satisfies Laplace's equation in the fluid domain

$$\mu^2\varphi_{xx} + \varphi_{zz} = 0 \quad (-D + \varepsilon h < z < \eta), \tag{2.1}$$

subject to the free-surface conditions

$$\left.\begin{aligned} &\varphi_z = \mu^2(1+\varphi_x)\eta_x \\ &\eta + \varphi_x + \frac{1}{2}\left(\varphi_x^2 + \varphi_z^2/\mu^2\right) = 0 \end{aligned}\right\} \quad (z = \eta), \tag{2.2}$$

and the bottom condition

$$\varphi_z = \mu^2(1+\varphi_x)\varepsilon h_x \quad (z = -D + \varepsilon h). \tag{2.3}$$

Here, μ, ε and D are the parameters defined in (1.1). In addition, we impose the radiation condition that waves appear downstream only

$$\varphi_x,\ \varphi_z,\ \eta \to 0 \quad (x \to -\infty). \tag{2.4}$$

2.2. *Hydraulic solution*

Focusing on the flow conditions (1.3), the first solution attempt is to expand φ and η in powers of μ^2:

$$\varphi = \varphi_0(x) + \mu^2\varphi_2(x, z) + \cdots, \qquad \eta = \eta_0(x) + \mu^2\eta_2(x) + \cdots. \tag{2.5}$$

Upon substituting these expansions in (2.1)–(2.3), the leading-order solution is

$$\eta_0 = -\varphi_{0x} - \frac{1}{2}\varphi_{0x}^2, \tag{2.6}$$

where $\varphi_0(x)$ is determined from the solvability of the $O(\mu^2)$ problem for $\varphi_2(x, z)$:

$$\varphi_{2zz} = -\varphi_{0xx} \quad (-D + \varepsilon h < z < \eta_0), \tag{2.7a}$$

$$\varphi_{2z} = (1+\varphi_{0x})\eta_{0x} \quad (z = \eta_0), \tag{2.7b}$$

$$\varphi_{2z} = (1+\varphi_{0x})\varepsilon h_x \quad (z = -D + \varepsilon h). \tag{2.7c}$$

https://doi.org/10.1017/jfm.2026.11312 Published online by Cambridge University Press

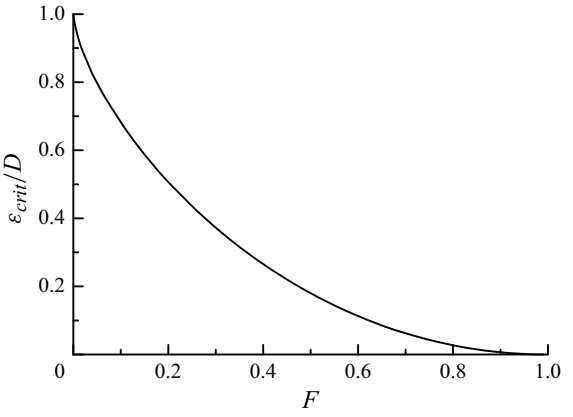


Figure 2. Plot of the critical topography height ε_{crit}/D as a function of the Froude number F according to (2.10).

Specifically, integrating (2.7*a*) across the fluid depth $-D+\varepsilon h<z<\eta_0$ along with the boundary conditions (2.7*b*, *c*) yields the conservation of mass flow rate

$$\frac{\mathrm{d}}{\mathrm{d}x}(\widetilde{U}\,\widetilde{D})=0, \tag{2.8}$$

where $\widetilde{U}(x)=1+\varphi_{0x}$ is the total horizontal velocity and $\widetilde{D}(x)=D+\eta_0-\varepsilon h$ is the local fluid depth (figure 1). Thus, upon invoking the upstream condition (2.4) and making use of (2.6), we obtain from (2.8)

$$\widetilde{U}^3+\widetilde{U}(2\varepsilon h-2D-1)+2D=0. \tag{2.9}$$

This cubic equation for $\widetilde{U}(x)$ governs the steady-state hydraulic solution.

Far upstream, where $\varepsilon h\to 0$, one of the three roots of (2.9) is $\widetilde{U}=1$, corresponding to the uniform stream; the other two (non-physical) roots are also real, one being larger than 1 (if $D>1$; i.e. the flow is subcritical, as assumed in (1.3)) and the other negative. As εh is increased, the physical root increases while the second positive root decreases, and these roots eventually merge to a double root, $\widetilde{U}=\widetilde{U}_{crit}$, for εh such that $\partial\widetilde{U}/\partial(\varepsilon h)\to\infty$. This defines a critical topography height $\varepsilon=\varepsilon_{crit}$ above which no physical root of (2.9) exists and, hence, no hydraulic steady state is possible. By imposing this criticality condition, it is readily found from (2.9) that (Long 1954)

$$\widetilde{U}_{crit}=F^{-2/3},\qquad \frac{\varepsilon_{crit}}{D}=1-\frac{3}{2}F^{2/3}+\frac{F^2}{2}. \tag{2.10}$$

Figure 2 shows a plot of ε_{crit}/D as a function of the Froude number F. It is seen that ε_{crit} is less than the fluid depth D, in keeping with the flow configuration in figure 1. In addition, $\varepsilon_{crit}\to 0$ when $F\to 1$, consistent with the fact that the linear steady-state response breaks down at the critical $F=1$.

We remark that the flow associated with the hydraulic steady state for $F<1$ is subcritical at all streamwise locations $-\infty<x<\infty$. Specifically, the local Froude number

$$\widetilde{F}(x)=\widetilde{U}(x)/\sqrt{\widetilde{D}(x)}<1. \tag{2.11}$$

https://doi.org/10.1017/jfm.2026.11312 Published online by Cambridge University Press

This certainly holds far upstream where $\varepsilon h \to 0$ so $\widetilde{F} = F < 1$. Additionally, $\widetilde{F}$ is an increasing function of εh (since $\widetilde{U}$ increases while $\widetilde{D}$ decreases as εh is increased) and, at the maximum topography height $\varepsilon = \varepsilon_{crit}$, $\widetilde{F} = 1$ from (2.6) and (2.10).

2.3. *Formulation in the wavenumber domain*

Carrying the expansions (2.5) in powers of μ to higher order cannot capture the wave response, as the wave amplitude is exponentially small with respect to μ. However, based on prior experience (KA2024, KA2025 and references therein), it is possible to diagnose the presence of radiating waves downstream by developing perturbation expansions in the wavenumber domain. For this purpose, rather than (2.1)–(2.3), we find it more convenient to use the non-local formulation of the water-wave problem (Ablowitz, Fokas & Musslimani 2006). In the present setting, this formulation leads to three nonlinear equations in integral form for $\eta(x)$, $u(x) = \varphi_x + \varphi_z \eta_x$ evaluated on the free surface $z = \eta$, and $w(x) = \varphi_x + \varphi_z \varepsilon h_x$ evaluated on the topography $z = -D + \varepsilon h$. Specifically,

$$\int_{-\infty}^{\infty} \mathrm{d}x \mathrm{e}^{-\mathrm{i}kx} \{(1+u)\sinh[\mu k(D+\eta)] - (1+w)\sinh[\mu k \varepsilon h(x)]\} = 0, \tag{2.12a}$$

$$\int_{-\infty}^{\infty} \mathrm{d}x \mathrm{e}^{-\mathrm{i}kx} \{(1+u)\cosh[\mu k(D+\eta)] - (1+w)\cosh[\mu k \varepsilon h(x)]\} = 0, \tag{2.12b}$$

$$\hat{\eta}(k) + \hat{u}(k) + \int_{-\infty}^{\infty} \mathrm{d}x \mathrm{e}^{-\mathrm{i}kx} \left\{ \frac{u^2}{2} - \frac{[(1+u)\mu\eta_x]^2}{2(1+\mu^2\eta_x^2)} \right\} = 0, \tag{2.12c}$$

where k is a (real) Fourier-like parameter and the Fourier transform in x is defined as

$$\hat{u}(k) = \frac{1}{2\pi} \int_{-\infty}^{\infty} u(x) \mathrm{e}^{-\mathrm{i}kx} \mathrm{d}x, \tag{2.13}$$

with analogous expressions for $\hat{\eta}$, $\hat{w}$ and $\hat{h}$.

For topography of infinitesimal height $\varepsilon \to 0$, linearizing the equation system (2.12) with respect to $(\hat{\eta}, \hat{u}, \hat{w}) = O(\varepsilon)$, yields $((\tanh \mu k D)/\mu k - 1)\hat{u} = \varepsilon \hat{h}\ \mathrm{sech}\mu k D$. Thus, $\hat{u}(k)$ has simple-pole singularities at $k = \pm\kappa_0/\mu$, where κ_0 solves

$$\tanh \kappa_0 D = \kappa_0. \tag{2.14}$$

For $F < 1$ $(D > 1)$, these poles are real. In addition, for smooth locally confined topography profile $h(x)$, the magnitude of $\hat{h}(\pm\kappa_0/\mu)$ is exponentially small with respect to μ. Thus, upon inverting the Fourier integrals (in keeping with (2.4)), the pole residues contribute a radiating wave downstream

$$u(x) \sim -\eta(x) \sim R \sin\left(\frac{\kappa_0}{\mu} x + \theta\right) \qquad (x \to \infty), \tag{2.15}$$

whose amplitude R is exponentially small with respect to μ.

When the topography has finite height $\varepsilon < \varepsilon_{crit}$, the ensuing asymptotic analysis for $\mu \ll 1$ shows that the location of the poles specified by (2.14), and hence the wavelength of the radiating wave above, persists. However, the wave amplitude R and the phase θ are controlled by a nonlinear beyond-all-orders mechanism. Importantly, for ε close to ε_{crit}, the exponentially small (with respect to μ) factor of R approaches $O(1)$.

https://doi.org/10.1017/jfm.2026.11312 Published online by Cambridge University Press

2.4. *Topography profile*

Kataoka & Akylas (2024) analysed the wave response due to small-height topography ($0 < \varepsilon \ll 1$). They assumed that the topography profile $h(x)$ is a smooth locally confined function that is even in x and whose (real) Fourier transform decays exponentially for large k, like

$$\hat{h}(k) \sim \left(A_0|k|^{\alpha} + \cdots\right) \exp(-\beta|k|) \quad (|k| \to \infty), \tag{2.16}$$

where A_0, α and β are real and $\beta > 0$.

The wave response due to finite-height topography ($\varepsilon < \varepsilon_{crit}$) requires fundamentally different treatment from KA2024. For convenience in presenting the analysis, here $h(x)$ is taken to have the specific Fourier transform

$$\hat{h}(k) = \frac{A_0}{2}\left(\frac{k}{\tanh(\pi k/2)}\right)^{\alpha} \operatorname{sech}\frac{\pi k}{2}. \tag{2.17}$$

This class of topography profiles (also used in KA2025) fits the asymptotic behaviour (2.16) with $\beta = \pi/2$. Here, α is a free parameter while A_0 is fixed by the normalization $h(0) = 1$ made earlier. (For $-30 < \alpha < 30$, it was checked numerically that $h(x)$, defined by (2.17), attains its maximum value at $x = 0$, but we have no proof that this holds for all α.) For the particular values $\alpha = 0$ and 1, the topography profiles corresponding to (2.17) are explicitly given by $h(x) = \operatorname{sech} x$ and $\operatorname{sech}^2 x$, respectively. Generalization of the present analysis to other locally confined topography profiles is possible as long as they are smooth and even in x (see comments in § 8).

3. Overview of exponential asymptotics

Before embarking on the detailed analysis, we outline the main steps of the exponential-asymptotics procedure for computing the radiating wave downstream under the flow conditions (1.3).

As noted earlier, perturbation expansions in powers of μ in the physical domain, like (2.5), give no sign of the wave response at any order of μ. This is in contrast to analogous expansions of $(\hat{u}, \hat{w}, \hat{\eta})$, which become disordered (non-uniform) at large wavenumber ($k \gg 1$) owing to the pole singularities at $k = \pm\kappa_0/\mu$ that give rise to the radiating wave (2.15). Here, it turns out that such non-uniformity first arises at $k = O(\mu^{-4/5})$ (see § 4.1). Accordingly, similar to 'two-timing' in studies of nonlinear oscillations, we introduce the 'stretched' wavenumber

$$K = \mu^{4/5} k \tag{3.1}$$

and propose the two-scale expansions

$$(\hat{u}, \hat{w}, \hat{\eta}) = \left(\hat{U}(K), \hat{W}(K), \hat{H}(K)\right)\mu^{6/5} \exp(-\gamma|k|) + \cdots, \tag{3.2}$$

valid for $K = O(1)$. Here, $(\hat{U}, \hat{W}, \hat{H})$ are $O(1)$ 'slowly varying' amplitudes, while $\exp(-\gamma|k|)$ is a 'fast' exponential that derives from the asymptotic behaviour for $|k| \gg 1$ of the Fourier transform of the hydraulic solution.

Next, we derive (approximate) equations for $(\hat{U}, \hat{W}, \hat{H})$ by substituting (3.2) into the water-wave equations (2.12) in the wavenumber domain (see § 4.2). In simpler problems (e.g. Akylas & Yang 1995; Kataoka & Akylas 2022), such amplitude equations suffice to compute the (exponentially small) residues of the simple poles associated with the radiating wave. The wave amplitude and phase then are determined by the contribution

https://doi.org/10.1017/jfm.2026.11312 Published online by Cambridge University Press

of these residues upon inverting the Fourier transforms. Here, however, the poles in (2.14) occur at $k = \pm\kappa_0/\mu$, whereas the expansions (3.2) hold only up to $K = O(1)$; i.e. $k = O(\mu^{-4/5}) \ll O(1/\mu)$. Thus, a separate, 'far-field' analysis for $k = O(1/\mu)$ is necessary in order to capture the wave response.

To this end, the equations for $(\hat{U}, \hat{W}, \hat{H})$ are solved in the limit $K \gg 1$ (see § 4.3). These asymptotic solutions later serve as matching conditions with an appropriate far-field solution (see § 5). This solution is obtained most conveniently in the physical domain, by returning to expansions (2.5) and including a short-scale wave train downstream (the terms in the curly brackets below)

$$\varphi(x, z) = \varphi_0(x) + \mu^2\varphi_2(x, z) + \cdots + \mu\left\{\Phi(x, z; \mu)\, \mathrm{e}^{\mathrm{i}\psi(x;\mu)/\mu} + \text{c.c.}\right\}, \tag{3.3a}$$

$$\eta(x) = \eta_0(x) + \mu^2\eta_2(x) + \cdots + \left\{Q(x; \mu)\, \mathrm{e}^{\mathrm{i}\psi(x;\mu)/\mu} + \text{ c.c.}\right\}. \tag{3.3b}$$

In these modified expansions, the short-scale wave train is modulated by the hydraulic disturbance ('long wave') present in the vicinity of the topography. Specifically, the phase function $\psi(x; \mu)$ describes the local wavenumber and Φ, Q are amplitude functions whose magnitude is expected to be exponentially small with respect to μ. Upon substituting (3.3) in the water-wave equations (2.1)–(2.3), ψ, Φ and Q are readily computed by standard modulation theory. This confirms that far downstream ($x \to \infty$) the short-scale disturbance is a uniform radiating wave train with wavenumber κ_0/μ, as claimed in (2.15). However, Φ, Q are proportional to a complex constant C, which still remains undetermined. Importantly, the magnitude and phase of C control the radiating wave amplitude R and phase θ in (2.15).

This missing link is provided by matching the far-field solution above with the two-scale expansions (3.2) (see § 6). Specifically, we match the Fourier transform of the short-scale modulated wave train in (3.3) with the asymptotic solution for $K \gg 1$ of $(\hat{u}, \hat{w}, \hat{\eta})$ in (3.2), found earlier. This matching is achieved in a certain overlap wavenumber range where both these solutions are valid asymptotically. As a result, we obtain an explicit expression for the constant C from which follow R and θ (viz. (6.3)).

4. Two-scale analysis in the wavenumber domain

Carrying out the programme outlined in § 3, here we focus on the water-wave equations (2.12) in the wavenumber domain. The goal is to obtain a uniformly valid approximation to $(\hat{u}, \hat{w}, \hat{\eta})$ for $|k| \gg 1$, which later (see § 6) will enable matching with the Fourier transform of the short-scale wave train downstream.

4.1. *Scalings*

We start by expanding $(\hat{u}, \hat{w}, \hat{\eta})$ in powers of μ^2,

$$\hat{u}(k; \mu) = \hat{u}_0(k) + \mu^2\hat{u}_2(k) + \cdots, \tag{4.1}$$

with analogous expressions for $\hat{w}$ and $\hat{\eta}$. While these straightforward expansions become disordered when $|k| \gg 1$, by examining this disordering at the first few orders of μ^2 we deduce the appropriate scalings of k and $(\hat{u}, \hat{w}, \hat{\eta})$ in the two-scale expansions (3.2). For this purpose, in (2.12) it is convenient to expand sinh, cosh and $(1 + \mu^2\eta_x^2)^{-1}$ in powers of μ^2k^2,

https://doi.org/10.1017/jfm.2026.11312 Published online by Cambridge University Press

$$\mathbb{F}[(1+u)(D+\eta-\varepsilon h)-D]=\mathbb{F}[(w-u)\varepsilon h]-\frac{\mu^2k^2}{6}\mathbb{F}\left[(1+u)\left((D+\eta)^3-(\varepsilon h)^3\right)\right]+O\left(\mu^4k^4\hat{u}\right), \tag{4.2a}$$

$$\mathbb{F}[w-u]=\frac{\mu^2k^2}{2}\mathbb{F}\left[(1+u)\left((D+\eta)^2-(\varepsilon h)^2\right)\right]+O\left(\mu^4k^4\hat{u}\right), \tag{4.2b}$$

$$\mathbb{F}\left[\eta+u+\frac{u^2}{2}\right]=\frac{\mu^2k^2}{2}\mathbb{F}\left[(1+u)^2\frac{\eta_x^2}{k^2}\right]+O\left(\mu^4k^4\hat{u}\right), \tag{4.2c}$$

where $\mathbb{F}[\,\cdot\,]$ denotes the Fourier transform as defined in (2.13).

Upon substituting (4.1) in (4.2), as expected, the leading-order solution $(\hat{u}_0, \hat{w}_0, \hat{\eta}_0)$ is the Fourier transform of the hydraulic solution (see § 2.2),

$$u_0=\varphi_{0x}, \qquad w_0=u_0, \qquad \eta_0=-u_0-\frac{1}{2}u_0^2, \tag{4.3}$$

where $u_0(x)$ is the perturbation horizontal velocity from the uniform stream, and the total horizontal velocity $\widetilde{U}(x)=1+u_0(x)$ satisfies the cubic (2.9). As discussed earlier, for $F<1$ steady state is possible only if $\varepsilon<\varepsilon_{crit}$, where $\varepsilon_{crit}(F)$ is given by (2.10) and is plotted in figure 2.

The behaviour of $(\hat{u}_0, \hat{w}_0, \hat{\eta}_0)$ as $|k|\to\infty$ is tied to the dominant singularities of (u_0, w_0, η_0). These singularities generally are of the branch-point type and are located on the imaginary axis closest to the origin of the complexified x-plane, say at $x=\pm\mathrm{i}\gamma$. To determine γ, there are two possible scenarios: (i) γ is a root of $\varepsilon h(\mathrm{i}\gamma)-\varepsilon_{crit}=0$ such that $\gamma<\pi/2$; (ii) $\gamma=\pi/2$. The latter possibility arises because $x=\pm\mathrm{i}\pi/2$ are the dominant singularities of $h(x)$ for the topography profiles chosen earlier (cf. (2.17)),

$$h(x)\sim\begin{cases}\dfrac{A_0\Gamma(\alpha+1)}{(\pi/2\pm\mathrm{i}x)^{\alpha+1}} & (\alpha>-1)\\ -A_0\ln(\pi/2\pm\mathrm{i}x) & (\alpha=-1)\end{cases}\qquad\left(x\to\pm\frac{\mathrm{i}\pi}{2}\right), \tag{4.4a}$$

$$\frac{\mathrm{d}^m h}{\mathrm{d}(\mp\mathrm{i}x)^m}\sim\frac{A_0\Gamma(\alpha+1+m)}{(\pi/2\pm\mathrm{i}x)^{\alpha+1+m}}\quad(\alpha<-1)\qquad\left(x\to\pm\frac{\mathrm{i}\pi}{2}\right), \tag{4.4b}$$

where m is the greatest integer less than or equal to $-\alpha$ and Γ is the gamma function. Which of (i) and (ii) is appropriate depends on α and ε, as discussed below.

When $\alpha\geq-1$, according to (4.4a), $h(x)\to\infty$ as $x\to\pm\mathrm{i}\pi/2$ from the origin along the imaginary x-axis. Since $h(0)=1$, this implies that $h(x)$ reaches $\varepsilon_{crit}/\varepsilon>1$ at some $x=\pm\,\mathrm{i}\gamma$, say, where $\gamma(\alpha,\varepsilon)<\pi/2$. Therefore, in this instance, scenario (i) above is valid for the entire range $0<\varepsilon<\varepsilon_{crit}$ of topography heights.

According to (2.10), at $x=\pm\mathrm{i}\gamma$, where $\varepsilon h=\varepsilon_{crit}$, the cubic (2.9) has a double root, $\widetilde{U}_{crit}=F^{-2/3}=D^{1/3}$. Thus, close to $x=\pm\mathrm{i}\gamma$,

$$\varepsilon h(x)=\varepsilon_{crit}\pm\frac{\varepsilon}{\mathrm{i}}\left.\frac{\mathrm{d}h}{\mathrm{d}x}\right|_{x=\pm\mathrm{i}\gamma}(\gamma\pm\mathrm{i}x)+\cdots, \tag{4.5a}$$

$$\widetilde{U}(x)=D^{1/3}-A\sqrt{\gamma\pm\mathrm{i}x}+B(\gamma\pm\mathrm{i}x)+\cdots. \tag{4.5b}$$

Upon substituting (4.5) in (2.9), collecting terms of equal order yields

$$A^2=\pm\frac{2\mathrm{i}}{3}\varepsilon\left.\frac{\mathrm{d}h}{\mathrm{d}x}\right|_{x=\pm\mathrm{i}\gamma}, \qquad B=\frac{A^2}{3D^{1/3}}. \tag{4.6}$$

https://doi.org/10.1017/jfm.2026.11312 Published online by Cambridge University Press

For certain values of α, including $\alpha = 0$ which corresponds to the topography $h = \operatorname{sech} x$ (used in the numerical computations in § 7), it is possible to find explicit expressions for γ and A. Generally, however, these constants are computed numerically by first determining $h(x)$ from $\hat{h}(k)$ in (2.17) and then solving $\varepsilon h(\mathrm{i}\gamma) - \varepsilon_{crit} = 0$.

Making use of (4.5) and (4.6), the behaviour of the hydraulic solution (4.3) near $x = \pm\mathrm{i}\gamma$ is

$$u_0(x) = w_0(x) \sim -1 + D^{1/3} - A\sqrt{\gamma \pm \mathrm{i}x} + \frac{A^2}{3D^{1/3}}(\gamma \pm \mathrm{i}x) + \cdots \quad (x \to \pm\mathrm{i}\gamma), \tag{4.7a}$$

$$\eta_0(x) \sim \frac{1 - D^{2/3}}{2} + D^{1/3}A\sqrt{\gamma \pm \mathrm{i}x} - \frac{5}{6}A^2(\gamma \pm \mathrm{i}x) + \cdots \quad (x \to \pm\mathrm{i}\gamma). \tag{4.7b}$$

Then, evaluating $(\hat{u}_0(k), \hat{w}_0(k), \hat{\eta}_0(k))$, these branch-point singularities make the dominant contribution as $|k| \to \infty$

$$\hat{u}_0(k) = \hat{w}_0(k) = -\frac{\hat{\eta}_0(k)}{D^{1/3}} \sim \frac{A}{2\sqrt{\pi}}|k|^{-3/2}\exp(-\gamma|k|) \quad (|k| \to \infty). \tag{4.8}$$

At $O(\mu^2)$ in expansion (4.1), the asymptotic behaviour of $\hat{u}_2(k)$ as $|k| \to \infty$ is controlled by the dominant singularities of $u_2(x)$. From (4.2), along with (4.5)–(4.7), it follows that (u_2, w_2, η_2) feature double poles at $x = \pm\mathrm{i}\gamma$ (see Appendix A),

$$u_2(x) = w_2(x) = -\frac{\eta_2(x)}{D^{1/3}} \sim \frac{D^{5/3}}{36(\gamma \pm \mathrm{i}x)^2} \quad (x \to \pm\mathrm{i}\gamma), \tag{4.9}$$

which yield

$$\hat{u}_2(k) = \hat{w}_2(k) = -\frac{\hat{\eta}_2(k)}{D^{1/3}} \sim \frac{D^{5/3}}{36}|k|\exp(-\gamma|k|) \quad (|k| \to \infty). \tag{4.10}$$

Finally, combining (4.8) and (4.10) with (4.1), it is found that

$$\hat{u}(k) = \hat{w}(k) = -\frac{\hat{\eta}(k)}{D^{1/3}} \sim \left\{\frac{A}{2\sqrt{\pi}}|k|^{-3/2} + \frac{\mu^2 D^{5/3}|k|}{36} + \cdots\right\}\exp(-\gamma|k|) \quad (|k| \to \infty). \tag{4.11}$$

Thus, expansion (4.1) becomes disordered when $k = O(\mu^{-4/5})$. This justifies the stretched wavenumber $K = \mu^{4/5}k$ in (3.1). Furthermore, for $K = O(1)$, (4.11) suggests replacing the 'naïve' expansion (4.1) with the two-scale expansion (3.2).

Coming now to the case $\alpha < -1$, $h(x)$ remains finite at $x = \pm\mathrm{i}\pi/2$ according to (4.4*b*). Therefore, starting at the origin where $h(0) = 1$, $\varepsilon h(\pm\mathrm{i}\gamma) = \varepsilon_{crit}$ can be met for $\gamma < \pi/2$ (scenario (i) above) only when

$$\varepsilon > \varepsilon_0 = \frac{\varepsilon_{crit}}{h(\pm\mathrm{i}\pi/2)}. \tag{4.12}$$

(For the $\hat{h}(k)$ in (2.17), it is straightforward to verify that $h(\mathrm{i}x)$ is monotonically increasing in $0 < x < \pi/2$.) Under condition (4.12), the dominant singularities of (u_0, w_0, η_0) are branch points at $x = \pm\mathrm{i}\gamma$ as in the case $\alpha > -1$, so (4.7) remain valid and the asymptotic behaviours (4.11) still hold. Thus, when $\varepsilon_0 < \varepsilon < \varepsilon_{crit}$, the two-scale expansions (3.2) also apply to $\alpha < -1$.

In contrast, for $\varepsilon < \varepsilon_0$, the dominant singularities are no longer branch points at $x = \pm\mathrm{i}\gamma$ ($\gamma < \pi/2$). Instead, the behaviour of $(\hat{u}(k), \hat{w}(k), \hat{\eta}(k))$ for $|k| \to \infty$ is controlled by the

https://doi.org/10.1017/jfm.2026.11312 Published online by Cambridge University Press

singularities of the topography profile at $x = \pm i\pi/2$ (scenario (ii) above). The case $\varepsilon < \varepsilon_0$ will not be pursued here (see KA2025 for detailed discussion of an analogous situation in a model problem).

4.2. *Amplitude equations*

The two-scale expansions (3.2) approximate $(\hat{u}, \hat{w}, \hat{\eta})$ for $1 \ll |k| = O(\mu^{-4/5})$ while the straightforward expansions (4.1) do so for $0 \leq |k| \ll \mu^{-4/5}$. In addition, these expansions should match for k in the overlap range

$$1 \ll |k| = O(1/\delta) \ll \mu^{-4/5}, \tag{4.13}$$

where δ is a constant such that $\mu^{4/5} \ll \delta \ll 1$. In view of (4.11), matching requires the amplitude functions $(\hat{U}(K), \hat{W}(K), \hat{H}(K))$ in (3.2) to satisfy

$$\hat{U}(K) = \hat{W}(K) = -\frac{\hat{H}(K)}{D^{1/3}} \sim \frac{A}{2\sqrt{\pi}}|K|^{-3/2} \quad (K \to 0). \tag{4.14}$$

We now derive the equations that govern $(\hat{U}, \hat{W}, \hat{H})$ for $0 < K = O(1)$. This involves substituting expansions (3.2) and (4.1) in the water-wave equations (4.2) and approximating the convolution integrals that arise from the Fourier transform of nonlinear terms. In carrying out these approximations, however, the singular behaviour as $K \to 0$ in (4.14) causes convergence problems. To bypass this difficulty, we subtract out this behaviour

$$\hat{u}(k;\, \mu) = \hat{u}_0(k) + \hat{u}_s(k;\, \mu) \tag{4.15}$$

(with analogous expressions for $\hat{w}(k;\, \mu)$ and $\hat{\eta}(k;\, \mu)$) and work with $(\hat{u}_s, \hat{w}_s, \hat{\eta}_s)$. Then, from (4.11) it follows that the corresponding two-scale expansions are in the same form as (3.2),

$$(\hat{u}_s, \hat{w}_s, \hat{\eta}_s) = (\hat{U}_s(K), \hat{W}_s(K), \hat{H}_s(K))\, \mu^{6/5} \exp(-\gamma|k|) + \cdots, \tag{4.16}$$

but the matching conditions for the amplitude functions are no longer singular,

$$\hat{U}_s(K) = \hat{W}_s(K) = -\frac{\hat{H}_s(K)}{D^{1/3}} \sim \frac{D^{5/3}}{36}|K| \quad (K \to 0). \tag{4.17}$$

Detailed derivation of the amplitude equations is given in Appendix B. The final result is that $\hat{U}_s(K)$ for $K > 0$ is governed by the Volterra-type integral equation

$$-\frac{K^2D^2}{3}\hat{U}_s(K) + 3D^{1/3}\int_0^K \left(\frac{A}{\sqrt{\pi}}\lambda^{-1/2}\frac{\mathrm{d}\hat{U}_s(K-\lambda)}{\mathrm{d}K} - \frac{\hat{U}_s(\lambda)\hat{U}_s(K-\lambda)}{2}\right)\mathrm{d}\lambda$$
$$= \frac{D^2A}{6\sqrt{\pi}}K^{1/2}, \tag{4.18}$$

subject to the matching condition (4.17). Once $\hat{U}_s(K)$ has been determined,

$$\hat{W}_s(K) = \hat{U}_s(K), \qquad \hat{H}_s(K) = -D^{1/3}\hat{U}_s(K). \tag{4.19}$$

It should be noted that the parameters A and D can be scaled out of (4.16) and (4.17) via

$$(K, \lambda, \hat{U}_s) \to \frac{A^{2/5}}{\pi^{1/5}}\left(D^{-2/3}K',\, D^{-2/3}\lambda',\, D\hat{U}_s'\right). \tag{4.20}$$

https://doi.org/10.1017/jfm.2026.11312 Published online by Cambridge University Press

This leads to the parameter-free equation (with primes dropped)

$$-\frac{K^2}{3}\hat{U}_s(K)+3\int_0^K\left(\lambda^{-1/2}\frac{\mathrm{d}\hat{U}_s(K-\lambda)}{\mathrm{d}K}-\frac{\hat{U}_s(\lambda)\hat{U}_s(K-\lambda)}{2}\right)\mathrm{d}\lambda=\frac{K^{1/2}}{6}, \tag{4.21}$$

and the matching condition

$$\hat{U}_s(K)\sim\frac{K}{36}\quad(K\to 0). \tag{4.22}$$

Thus, upon solving (4.21) subject to (4.22), the scaling (4.20) determines $\hat{U}_s(K)$ for all topography profiles $h(x)$ defined by (2.17).

4.3. *Asymptotic solution for $K\gg 1$*

In preparation for matching with the far-field solution, we now examine the asymptotic behaviour of $\hat{U}_s(K)$ for $K\gg 1$. The integral equation (4.21) subject to condition (4.22) has precisely the form of an amplitude equation analysed in KA2025 (their equation (3.11) subject to their condition (3.6)). Following the same procedure as in KA2025, we find

$$\hat{U}_s(K)\sim C_0K\exp\left(\frac{K^5}{405\pi}\right)\quad(K\to\infty), \tag{4.23}$$

where

$$C_0\approx 0.061. \tag{4.24}$$

Then, reverting to the original variables in (4.20), this asymptotic solution reads

$$\hat{U}_s(K)\sim C_0D^{5/3}K\exp\left(\frac{D^{10/3}}{405A^2}K^5\right)\quad(K\to\infty) \tag{4.25}$$

with $\hat{W}_s(K)$ and $\hat{H}_s(K)$ given by (4.19).

It should be noted that, when k is near the expected pole of $\hat{u}(k)$ at κ_0/μ (cf. (2.14)), so $K=\mu^{4/5}k=O(\mu^{-1/5})\gg 1$, the exponent above is $O(1/\mu)$. However, the exponent of the fast exponential $\exp(-\gamma|k|)$ is $O(1/\mu)$ as well. This violates the separation of scales assumed in the two-scale expansions (4.16) and necessitates a rescaled, far-field analysis for $\kappa=\mu k=O(1)$. The behaviour of $\hat{U}_s(K)$ for $K\gg 1$ in (4.25) then enables matching to the far-field solution for $\kappa\ll 1$. These issues are discussed in §§ 5, 6.

5. Far-field analysis

Here, we construct a far-field solution that accounts for the radiating wave. This solution is obtained in the physical domain and then we compute its Fourier transform in preparation for matching with the asymptotic behaviour (4.25).

5.1. *Downstream wave response in the physical domain*

Returning to expansions (3.3), first we consider the long wave, represented by the terms outside the curly brackets. The leading-order solution is the hydraulic state (see § 2.2), and the inhomogeneous problem (2.7) for the $O(\mu^2)$ correction is readily solved (as the solvability condition (2.8) is already satisfied)

$$\varphi_2=\overline{\varphi}_2(x)-\widetilde{U}_x\frac{z^2}{2}+\left(\widetilde{U}\eta_0\right)_x z, \tag{5.1}$$

where $\overline{\varphi}_2(x)$ is an undetermined function of x.

https://doi.org/10.1017/jfm.2026.11312 Published online by Cambridge University Press

Next, we focus on the short-scale wave train in expansions (3.3), anticipating that its amplitude is exponentially small with respect to μ. Upon substituting (3.3) in the water-wave equations (2.1)–(2.3), collecting terms proportional to $\exp(\mathrm{i}\psi/\mu)$ yields, correct to $O(\mu|\Phi|)$,

$$\Phi_{zz} - \psi_x^2\Phi = -\mathrm{i}\mu(\psi_{xx}\Phi + 2\psi_x\Phi_x) \quad (-D+\varepsilon h < z < \eta_0), \tag{5.2}$$

$$\Phi_z - \psi_x^2\widetilde{U}^2\Phi = \mathrm{i}\mu\left\{\psi_x\eta_{0x}\Phi - \psi_x\widetilde{U}^2\left(\Phi|_{z=\eta_0}\right)_x - \left(\frac{\Phi_z|_{z=\eta_0}}{\psi_x}\right)_x\right\} \quad (z=\eta_0), \tag{5.3}$$

$$\Phi_z = \mathrm{i}\mu\psi_x\varepsilon h_x\Phi \quad (z=-D+\varepsilon h). \tag{5.4}$$

In addition,

$$Q = -\mathrm{i}\psi_x\widetilde{U}\Phi - \mu(\widetilde{U}\Phi_x + \varphi_{2z}\Phi_z) \quad (z=\eta_0). \tag{5.5}$$

The problem (5.2)–(5.4) is solved by expanding

$$\Phi(x,z;\mu) = \Phi_0(x,z) + \mu\Phi_1(x,z) + \cdots, \tag{5.6}$$

with

$$\psi(x;\mu) = \psi_0(x) + \mu\psi_1(x) + \cdots. \tag{5.7}$$

Substituting (5.6)–(5.7) in (5.2)–(5.4), the leading-order solution is governed by

$$\Phi_{0zz} - \tilde{\kappa}^2\Phi_0 = 0 \quad (-D+\varepsilon h < z < \eta_0), \tag{5.8}$$

$$\Phi_{0z} - \tilde{\kappa}^2\widetilde{U}^2\Phi_0 = 0 \quad (z=\eta_0), \tag{5.9}$$

$$\Phi_{0z} = 0 \quad (z=-D+\varepsilon h). \tag{5.10}$$

Hence,

$$\Phi_0 = C\cosh\{\tilde{\kappa}(x)(z+D-\varepsilon h)\}, \tag{5.11}$$

where C is an undetermined (complex) constant. In addition, ψ_0 is given by

$$\psi_0 = \int_0^x \tilde{\kappa}(x')\mathrm{d}x', \tag{5.12}$$

where $\tilde{\kappa}(x)/\mu$ is the local wavenumber of the short-scale wave train in keeping with the local dispersion relation

$$\frac{\tanh(\tilde{\kappa}\widetilde{D})}{\tilde{\kappa}} = \widetilde{U}^2, \tag{5.13}$$

with $\widetilde{D}(x) = D + \eta_0 - \varepsilon h$ being the local fluid depth in the hydraulic state. As the local Froude number is subcritical (cf. (2.11)), $\tilde{\kappa}(x)$ is real.

Proceeding to $O(\mu)$ in expansions (5.6)–(5.7), Φ_1 satisfies the inhomogeneous boundary-value problem

$$\Phi_{1zz} - \tilde{\kappa}^2\Phi_1 = I_1C \quad (-D+\varepsilon h < z < \eta_0), \tag{5.14}$$

$$\Phi_{1z} - \tilde{\kappa}^2\widetilde{U}^2\Phi_1 = I_2C \quad (z=\eta_0), \tag{5.15}$$

$$\Phi_{1z} = I_3C \quad (z=-D+\varepsilon h), \tag{5.16}$$

https://doi.org/10.1017/jfm.2026.11312 Published online by Cambridge University Press

with

$$I_1 = (2\tilde{\kappa}\psi_{1x} - \mathrm{i}\tilde{\kappa}_x)\cosh\{\tilde{\kappa}(z+D-\varepsilon h)\} \\ - 2\mathrm{i}\tilde{\kappa}\,\{\tilde{\kappa}_x(z+D-\varepsilon h) - \tilde{\kappa}\varepsilon h_x\}\sinh\{\tilde{\kappa}(z+D-\varepsilon h)\}, \tag{5.17a}$$

$$I_2 = 2\psi_{1x}\sinh(\tilde{\kappa}\widetilde{D}) - \mathrm{i}\tilde{\kappa}\widetilde{U}\left\{\widetilde{U}\cosh(\tilde{\kappa}\widetilde{D})\right\}_x - \mathrm{i}\left\{\sinh(\tilde{\kappa}\widetilde{D})\right\}_x, \tag{5.17b}$$

$$I_3 = \mathrm{i}\tilde{\kappa}\varepsilon h_x. \tag{5.17c}$$

Since the corresponding homogeneous problem has a solution, namely (5.11), the forcing terms I_1–I_3 above must observe a certain constraint in order for the problem (5.14)–(5.16) to have a solution as well. This solvability condition is deduced by multiplying (5.14) with Φ_0 in (5.11) and integrating across the fluid depth $-D+\varepsilon h < z < \eta_0$. After two integrations by parts and making use of the boundary conditions (5.15) and (5.16), one obtains

$$\int_{-D+\varepsilon h}^{\eta_0} I_1\cosh\{\tilde{\kappa}(z+D-\varepsilon h)\}\,\mathrm{d}z - I_2\cosh(\tilde{\kappa}\widetilde{D}) + I_3 = 0. \tag{5.18}$$

Inserting (5.17) in (5.18) and using (5.13), it follows that ψ_1 satisfies

$$\Omega(\tilde{\kappa}\widetilde{D})\,\psi_{1x} - \frac{\mathrm{i}}{2}\left\{\Omega(\tilde{\kappa}\widetilde{D})\right\}_x = 0, \tag{5.19}$$

where

$$\Omega(\tilde{\kappa}\widetilde{D}) \equiv \sinh(\tilde{\kappa}\widetilde{D})\cosh(\tilde{\kappa}\widetilde{D}) - \tilde{\kappa}\widetilde{D}. \tag{5.20}$$

Hence,

$$\mathrm{i}\psi_1 = -\frac{1}{2}\ln\frac{\Omega(\tilde{\kappa}\widetilde{D})}{\Omega(\kappa_0 D)}. \tag{5.21}$$

As $\mathrm{i}\psi_1(x)$ is real, $\exp(\mathrm{i}\psi_1)$ adds to the modulation of the short-wave amplitude in expansions (3.3). In fact, (5.19) written in the form

$$\frac{\mathrm{d}}{\mathrm{d}x}\left\{\Omega(\tilde{\kappa}\widetilde{D})\exp(2\mathrm{i}\psi_1)\right\} = 0 \tag{5.22}$$

can be shown to be equivalent to conservation of wave action in the steady modulated wave train downstream (Whitham 1974).

Combining (5.6), (5.7), (5.11), (5.12) and (5.21), the terms pertaining to the short-scale wave train in (3.3) take the form

$$\Phi\mathrm{e}^{\mathrm{i}\psi/\mu} = C\cosh\{\tilde{\kappa}(z+D-\varepsilon h)\}\sqrt{\frac{\Omega(\kappa_0 D)}{\Omega(\tilde{\kappa}\widetilde{D})}}\exp\left\{\frac{\mathrm{i}}{\mu}\int_0^x\tilde{\kappa}(x')\mathrm{d}x'\right\} + \cdots, \tag{5.23a}$$

$$Q\mathrm{e}^{\mathrm{i}\psi/\mu} = -\mathrm{i}C\tilde{\kappa}\widetilde{U}\cosh(\tilde{\kappa}\widetilde{D})\sqrt{\frac{\Omega(\kappa_0 D)}{\Omega(\tilde{\kappa}\widetilde{D})}}\exp\left\{\frac{\mathrm{i}}{\mu}\int_0^x\tilde{\kappa}(x')\mathrm{d}x'\right\} + \cdots. \tag{5.23b}$$

Far downstream ($x\to\infty$), the topography $\varepsilon h\to 0$ and the hydraulic state approaches the uniform stream ($\widetilde{U}\to 1$). As a result, according to (5.13), $\tilde{\kappa}(x)\to\kappa_0$ where κ_0 (>0) solves (2.14). Thus, making use of (5.23), the short-scale wave component in (3.3)

https://doi.org/10.1017/jfm.2026.11312 Published online by Cambridge University Press

approaches a uniform sinusoidal wave train

$$u(x) \sim \varphi_x|_{z=\eta_0}\ (\sim -\eta(x)) \sim 2\kappa_0|C|\cosh(\kappa_0 D) \times \sin\left\{\frac{\kappa_0}{\mu}x + \frac{1}{\mu}\int_0^\infty \left(\tilde{\kappa}(x') - \kappa_0\right)\mathrm{d}x' + \arg(-C)\right\} \quad (x \to \infty), \tag{5.24}$$

where $C = |C|\exp(\mathrm{i}\arg C)$. Furthermore, upon comparing (5.24) with (2.15), the radiating wave amplitude R and phase shift θ are related to C via

$$R = 2\kappa_0|C|\cosh(\kappa_0 D), \qquad \theta = \frac{1}{\mu}\int_0^\infty \left(\tilde{\kappa}(x') - \kappa_0\right)\mathrm{d}x' + \arg(-C). \tag{5.25}$$

5.2. *Far-field solution in the wavenumber domain*

We now compute the Fourier transform of the downstream modulated short-scale wave train found above. Specifically, using (5.23) in (3.3),

$$\hat{u} = \mathbb{F}\left[(\varphi_x + \varphi_z\eta_x)|_{z=\eta}\right] \sim \frac{C}{2\pi}\int_{-\infty}^{\infty} \mathrm{i}\tilde{\kappa}\cosh(\tilde{\kappa}\widetilde{D})\sqrt{\frac{\Omega(\kappa_0 D)}{\Omega(\tilde{\kappa}\widetilde{D})}}\exp\left\{\mathrm{i}\left(-kx + \frac{1}{\mu}\int_0^x \tilde{\kappa}(x')\mathrm{d}x'\right)\right\}\mathrm{d}x. \tag{5.26}$$

It should be noted that, of the two terms which are complex conjugate of each other in the curly brackets in (3.3), only the one $\propto \exp(\mathrm{i}\psi/\mu)$ is included above, as the corresponding local wavenumber $\tilde{\kappa}/\mu > 0$. Thus, only this term is appropriate for matching with (4.25), which was derived for $K > 0$.

In view of (4.7) and (5.13), the integrand in (5.26) features branch points at the zeroes of $\tilde{\kappa}(x)$, i.e. $x = \pm\mathrm{i}\gamma$. Accordingly, we introduce a branch cut between these two points on the imaginary x-axis, and deform the integration path to pass below $x = -\mathrm{i}\gamma$ (see figure 2 of KA2025). Furthermore, due to the radiation condition (2.4), the radiating wave train stretches only downstream ($\mathrm{Re}\, x > 0$) so the lower integration limit is replaced by $-\mathrm{i}\gamma$.

Next, we examine the asymptotic behaviour of the resulting contour integral

$$\hat{u} \sim \frac{C}{2\pi}\int_{-\mathrm{i}\gamma}^{\infty} \mathrm{i}\tilde{\kappa}\cosh(\tilde{\kappa}\widetilde{D})\sqrt{\frac{\Omega(\kappa_0 D)}{\Omega(\tilde{\kappa}\widetilde{D})}}\exp\left\{\frac{\mathrm{i}}{\mu}\left(-\kappa x + \int_0^x \tilde{\kappa}(x')\mathrm{d}x'\right)\right\}\mathrm{d}x, \tag{5.27}$$

when $\kappa = \mu k$ satisfies

$$\mu^{1/5} \ll \kappa \ll 1. \tag{5.28}$$

In terms of $K = \mu^{4/5}k$, this wavenumber range translates to $1 \ll K \ll \mu^{-1/5}$, so it is a common range of validity of the far-field solution (5.27) and the asymptotic solution (4.25) obtained earlier using the two-scale expansions (4.16). Therefore, these two solutions should match in the wavenumber range (5.28).

For κ satisfying (5.28), the integral in (5.27) is approximated following the procedure used for an analogous integral in KA2025 (see their (4.10)). Specifically, we first expand the integrand around the branch point $x = -\mathrm{i}\gamma$ and then evaluate the resulting integral asymptotically for $\kappa^5/\mu \gg 1$ using Laplace's method (see Appendix C). The final result is

https://doi.org/10.1017/jfm.2026.11312 Published online by Cambridge University Press

$$\hat{u} \sim -\frac{C}{3}\sqrt{\frac{\mu}{3\pi}\Omega(\kappa_0 D)}\,\frac{D^{2/3}}{A}\,\kappa\,\exp\left(-\frac{\mathrm{i}}{\mu}\int_{-\mathrm{i}\gamma}^{0}\tilde{\kappa}(x')\mathrm{d}x'\right)\exp\left(\frac{D^{10/3}}{405\mu A^2}\kappa^5\right)\mathrm{e}^{-\gamma k}$$
$$\left(\mu^{1/5} \ll \kappa \ll 1\right). \tag{5.29}$$

6. Radiating wave

We now compute the radiating wave amplitude and phase. Returning to the two-scale expansions (4.16) and making use of the asymptotic solution (4.25) for $\hat{U}_s(K)$, yields

$$\hat{u}_s \sim \mu^{6/5} C_0 D^{5/3} K \exp\left(\frac{D^{10/3}}{405A^2}K^5\right)\mathrm{e}^{-\gamma k} \quad \left(1 \ll K \ll \mu^{-1/5}\right). \tag{6.1}$$

In fact, this asymptotic result also applies to $\hat{u} = \hat{u}_0 + \hat{u}_s$ (cf. (4.15)) because, in view of (4.8), $\hat{u}_0$ is subdominant relative to $\hat{u}_s$ above. Thus, expression (6.1), written in terms of $\kappa = \mu^{1/5}K$, should match with expression (5.29) because the two-scale expansion (4.16) and the far-field solution (5.27) are both valid in the wavenumber range (5.28), as argued earlier. This matching requirement determines the constant C:

$$C = -3\sqrt{\frac{3\pi\mu}{\Omega(\kappa_0 D)}}\,C_0 A D \exp\left(\frac{\mathrm{i}}{\mu}\int_{-\mathrm{i}\gamma}^{0}\tilde{\kappa}(x')\mathrm{d}x'\right). \tag{6.2}$$

Then, the radiating wave amplitude and phase follow from (5.25),

$$R = 6\sqrt{\frac{3\pi\mu}{\Omega(\kappa_0 D)}}\,C_0 A D \kappa_0 \cosh(\kappa_0 D)\exp\left(-\frac{q(\alpha,\varepsilon)}{\mu}\right), \tag{6.3a}$$

$$\theta = \frac{1}{\mu}\int_0^\infty (\tilde{\kappa}(s) - \kappa_0)\,\mathrm{d}s, \tag{6.3b}$$

where C_0 is given by (4.24) and

$$q(\alpha,\varepsilon) = \int_0^\gamma \tilde{\kappa}(\mathrm{i}s)\mathrm{d}s. \tag{6.4}$$

It should be noted that $q(\alpha,\varepsilon)$ is real because $\tilde{\kappa}(x)$ is an even function according to (5.13). Furthermore, $q(\alpha,\varepsilon) > 0$ since $\tilde{\kappa}(x) > 0$ when $x = \mathrm{i}s$ $(0 < s < \gamma)$.

Figure 3 plots q as a function of $0 < \varepsilon < \varepsilon_{crit}$ when $F = 0.5$ $(D = 4)$ and for $\alpha = 1, 0$ and -0.5. It is seen that q decreases monotonically, so the exponential factor of R in (6.3*a*) grows with increasing ε. Thus, finite-height topography can enhance exponentially the radiating downstream wave. In addition, according to (6.3*b*), the phase shift θ is controlled by the deviation of the local wavenumber from its constant value far downstream, $(\tilde{\kappa} - \kappa_0)/\mu$. For $\varepsilon \to 0$, $\tilde{\kappa} \to \kappa_0$ according to (5.13), so (6.3*b*) recovers the linear result $\theta = 0$ (cf. (6.6)).

Importantly, when ε approaches ε_{crit}, the roots $x = \pm\mathrm{i}\gamma$ of $\varepsilon h(x) - \varepsilon_{crit} = 0$ approach the origin $(\gamma \to 0)$. Thus, according to (6.4) and as shown in figure 3,

$$q(\alpha,\varepsilon) \to 0 \quad (\varepsilon \to \varepsilon_{crit}), \tag{6.5}$$

so the exponential factor of R approaches $O(1)$. Even though the present theory formally breaks down in this limit, one still expects R to increase rapidly as $\varepsilon \to \varepsilon_{crit}$, resulting in a steep wave train downstream. It should be noted that this perhaps unexpected effect (confirmed by numerical computations in § 7) arises, however small μ (which controls dispersion) may be.

https://doi.org/10.1017/jfm.2026.11312 Published online by Cambridge University Press

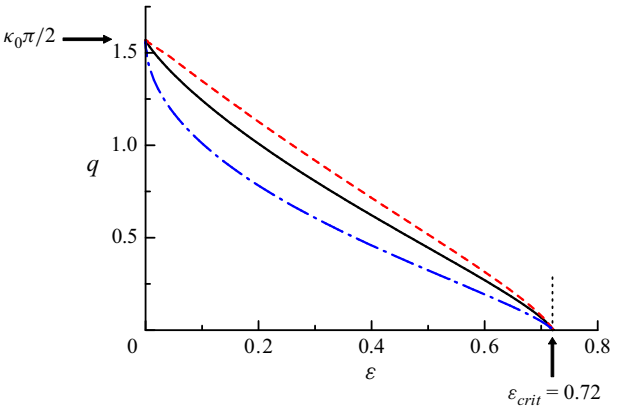


Figure 3. The exponent q (defined in (6.4)) that controls the exponential factor of the wave amplitude R, as a function of the peak topography height ε, when $F = 0.5$ ($D = 4$): $\alpha = 1$ (blue dash-dotted line); 0 (black solid line); -0.5 (red dashed line). The vertical dotted line indicates the critical topography height $\varepsilon_{crit} = 0.72$.

In the other extreme, when the topography height $\varepsilon \to 0$, the roots $x = \pm i\gamma$ of $\varepsilon h(x) - \varepsilon_{crit} = 0$ approach $x = \pm i\pi/2$ ($\gamma \to \pi/2$), where $h(x) \to \infty$ according to (4.4*a*). Furthermore, from (5.13), $\tilde{\kappa} \to \kappa_0$, so $q \to \kappa_0\pi/2$ (figure 3). Thus, the leading-order exponential factor $R = O(\exp(-\kappa_0\pi/2\mu))$ in (6.3*a*) is set by the behaviour of $\hat{h}(k)$ for $|k| \to \infty$ in (2.16), regardless of the peak topography height ε. This agrees with the classical linear solution for $\varepsilon \to 0$,

$$R_{lin} = \frac{4\pi\varepsilon A_0}{\mu^{\alpha+1}} C_{lin} \exp\left(\frac{-\kappa_0\pi}{2\mu}\right), \qquad \theta_{lin} = 0, \tag{6.6a}$$

where

$$C_{lin} = \frac{2\kappa_0^{\alpha+1} \sinh \kappa_0 D}{\sinh 2\kappa_0 D - 2\kappa_0 D}, \tag{6.6b}$$

as well as with the wave response for topography of small height $0 < \varepsilon \ll 1$ (KA2024). In the latter case, however, the wave amplitude (save for the leading-order exponential factor) is controlled by a nonlinear mechanism.

It should be noted that, while the exponential factor in (6.3*a*) reduces for $0 < \varepsilon \ll 1$ to that found in KA2024, the asymptotic solutions for small- and finite-height topography do not merge smoothly. To handle this difficulty, an 'intermediate' solution that takes into account the effects of the nearly coalescing singularities at $x = \pm i\gamma$ and $x = \pm i\pi/2$, would be needed. Treating problems with coalescing singularities via exponential asymptotics was discussed in Trinh & Chapman (2015).

7. Numerical results

We now turn to direct numerical computations based on the full water-wave equations in order to assess the validity of the asymptotic theory. Additionally, motivated by the asymptotic results, we investigate numerically the appearance of steep waves downstream when $\varepsilon \approx \varepsilon_{crit}$.

Our computations used the boundary-integral method of Belward & Forbes (1993) for steady two-layer flow over topography (setting the upper-layer density to zero in their formulation). We employed uniform computational meshes, typically for $-25D < x/\mu < 40D$ and allocating 25 discrete points to each wavelength of the downstream wave.

https://doi.org/10.1017/jfm.2026.11312 Published online by Cambridge University Press

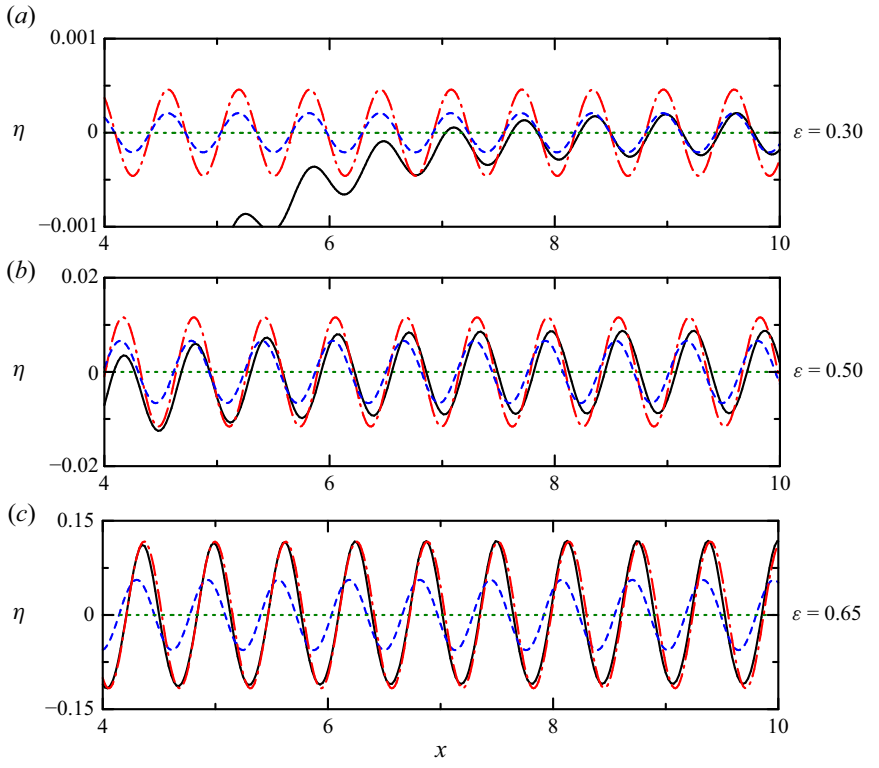


Figure 4. Downstream wave profiles $\eta(x)$ in free-surface flow over topography with $h(x) = \mathrm{sech}x$ and peak height (*a*) $\varepsilon = 0.30$, (*b*) 0.50 and (*c*) 0.65, when $F = 0.5$ ($D = 4$) and $\mu = 0.1$: exact numerical solution (black solid line); finite-height theory (6.3) (red dash-dotted line); small-height theory (blue dashed line); linear theory (6.6) (green dotted line).

In the interest of brevity, here we report on numerical computations only for the topography profile $h(x) = \mathrm{sech}\, x$ (corresponding to $\alpha = 0$, $A_0 = 1$ in (2.17)). In this instance, there are explicit expressions for the parameters γ and A in (4.5)–(4.6):

$$\gamma = \cos^{-1}\left(\frac{\varepsilon}{\varepsilon_{crit}}\right), \qquad A = \sqrt{\frac{2\varepsilon_{crit}}{3}}\left\{\left(\frac{\varepsilon_{crit}}{\varepsilon}\right)^2 - 1\right\}^{1/4}. \tag{7.1}$$

Furthermore, the Froude number is fixed to $F = 0.5$ ($D = 4$), which specifies $\varepsilon_{crit} = 0.72$ according to (2.10). Our results for other values of $\alpha > -1$ and $F < 1$ are qualitatively similar to those discussed below.

Figure 4 plots theoretical and numerically computed downstream wave profiles for $\mu = 0.1$ and topography peak heights $\varepsilon = 0.30$, 0.50 and 0.65. It is noted that the largest of these, ε, is not far from $\varepsilon_{crit} = 0.72$. The theoretical wave profiles in figure 4 are the predictions of the finite-height theory (6.3), the small-height theory (obtained from (5.13) in KA2024 by multiplying R with ε and setting $n = 0$) and the linear response (6.6) (with $\alpha = 0$, $A_0 = 1$).

Figure 4 shows that the small-height theory is most accurate for the smallest of the three topography heights, $\varepsilon = 0.30$, while the finite-height theory works best for the largest, $\varepsilon = 0.65$. For the intermediate $\varepsilon = 0.50$, which falls in the transition range from the small- to the finite-height solution, both these solutions provide reasonably good, but not excellent, approximations to the radiating wave. By contrast, the linear solution grossly

https://doi.org/10.1017/jfm.2026.11312 Published online by Cambridge University Press

underestimates the wave response for all three values of ε. Specifically, for $\varepsilon = 0.30$, the small-height theoretical predictions for the wave amplitude R and the phase shift θ agree very well with the numerical solution while the finite-height solution clearly overestimates R (by roughly a factor of 2). On the other hand, for $\varepsilon = 0.65$, the finite-height theoretical predictions for R and θ are in excellent agreement with the numerical solution, unlike the small-height solution which underestimates R (by roughly a factor of 0.5) and also exhibits a noticeable phase lag relative to the numerical wave profile.

In figure 5, we compare theoretical with numerical results for the ratio of the nonlinear to the linear wave amplitude R/R_{lin} as a function of the topography peak height $0 < \varepsilon < \varepsilon_{crit} = 0.72$, for three values of $\mu = 0.1$, 0.15 and 0.2. As expected, the agreement of asymptotic with numerical results improves as μ is decreased. Furthermore, the small-height theory (KA2024) provides a reliable approximation for $0 < \varepsilon \lesssim 0.5$ (see the insets in figure 5) while the finite-height result (6.3*a*) does so for $0.5 < \varepsilon < \varepsilon_{crit}$. However, as noted earlier, the small- and finite-height asymptotic results do not merge smoothly.

Figure 5 indicates that the radiating wave amplitude R increases rapidly when ε approaches ε_{crit}. In this limit, in view of (6.5), the exponentially small factor of R in (6.3*a*) becomes $O(1)$ and our exponential-asymptotics procedure breaks down. Additionally, the steady hydraulic solution (4.3), which forms the starting point of the present analysis, is not valid when $\varepsilon > \varepsilon_{crit}$. Accordingly, below we explore by numerical means the behaviour of the downstream wave for $\varepsilon \approx \varepsilon_{crit}$.

Figure 6 plots numerical results for the downstream wave amplitude R, defined as half the crest-to-trough height, as a function of the topography peak height ε in the vicinity of ε_{crit}, for three values of $\mu = 0.05$, 0.1 and 0.2. These results indicate that for each μ there is a limiting topography height, ε_{lim}, beyond which no steady wave train can be computed. Furthermore, as μ is decreased, ε_{lim} approaches ε_{crit}. (While $\varepsilon_{lim} < \varepsilon_{crit}$ in figure 6, computations for other F and μ, not shown here, indicate that ε_{lim} can exceed ε_{crit}.)

According to figure 6, as ε approaches ε_{lim}, R increases dramatically and reaches $O(1)$, suggesting that the wave train downstream becomes fully nonlinear. This is confirmed in figure 7, which displays the computed free-surface profile for $\mu = 0.1$ and ε slightly below 0.70, the value of ε_{lim} for this μ. Indeed, the wave downstream has steep crests and broad troughs, resembling a steep Stokes wave. Naturally, these nonlinear features are not captured by our exponential-asymptotics theory. Nevertheless, the present theory does hint at the rapid increase of the wave amplitude as ε approaches $\varepsilon_{lim} \approx \varepsilon_{crit}$ for $\mu \ll 1$. Figure 6 also indicates the limiting amplitude R_{lim} of steady Stokes periodic waves for $D = 4$ (which essentially corresponds to deep water), as estimated from the numerical computations of Williams (1981). As expected, R_{lim} provides an upper bound for R, and the computed wave downstream for ε slightly below ε_{lim} (figure 7) is close to the limiting Stokes wave.

Finally, we discuss briefly the wave response when the peak topography height ε exceeds ε_{lim}, so no steady solution can be computed. Instead, an initial-value problem was solved starting from rest and turning on the uniform stream impulsively, based on the time-dependent water-wave equations. This unsteady flow was computed using the numerical method of Dold & Peregrine (1986), which can handle breaking waves. This method introduces fluid particles on the free surface and their motion is determined by integrating the Lagrangian time derivatives of their positions. We used approximately 35 particles per wavelength of the downstream wave, with 2000 particles in total. This resolution enabled us to capture with sufficient accuracy the overhanging motion of a crest. The time step (using U_*/g as the time scale) was initially set to $\triangle t = 0.1$ and then reduced to $\triangle t = 0.01$ once an overhanging crest appeared. As a check, the numerical procedure was applied to the initial-value problem for values of $\varepsilon < \varepsilon_{lim}$ and it was verified that the flow approached the steady state computed earlier.

https://doi.org/10.1017/jfm.2026.11312 Published online by Cambridge University Press

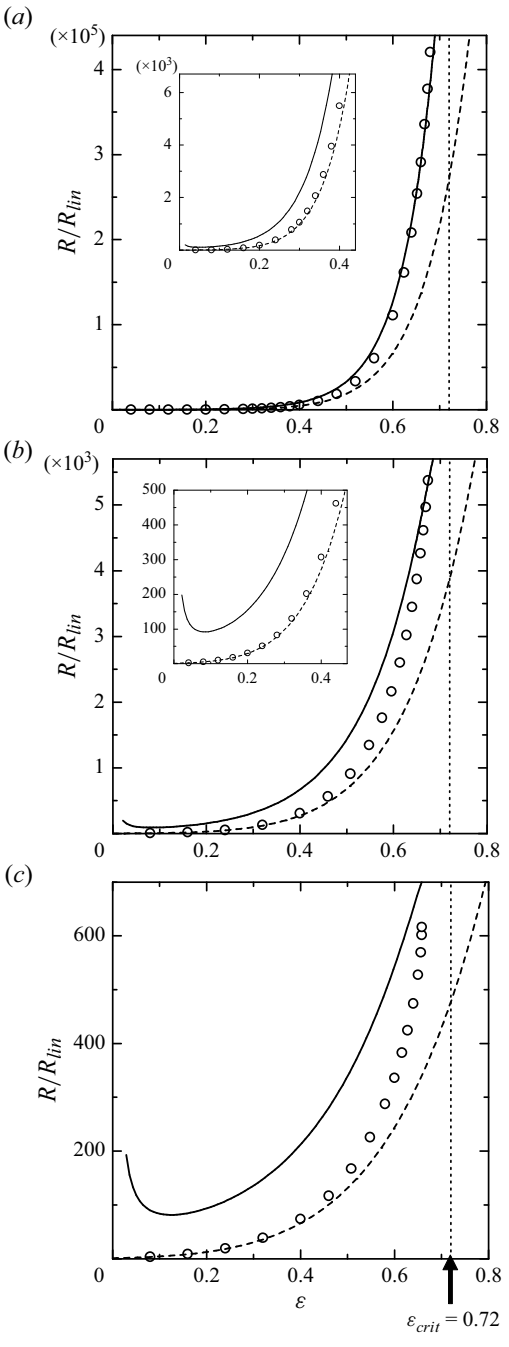


Figure 5. Ratio of nonlinear to linear wave amplitude as a function of the topography peak height. Here (*a*) $\mu = 0.1$, (*b*) 0.15 and (*c*) 0.2: exact numerical solution (circle); finite-height theory (6.3) (solid line); small-height theory (dashed line). The insets zoom in on $\varepsilon \ll 1$. The vertical dotted lines denote the critical height $\varepsilon_{crit} = 0.72$ (cf. (2.10)).

Figure 8 shows the computed unsteady free-surface profile for $\mu = 0.1$ and $\varepsilon = 0.76 > \varepsilon_{lim} = 0.70$, at $t = 107$. At this time, an 'undular bore' with steep crests has formed downstream of the topography and one of these crests is starting to overhang, signalling

https://doi.org/10.1017/jfm.2026.11312 Published online by Cambridge University Press

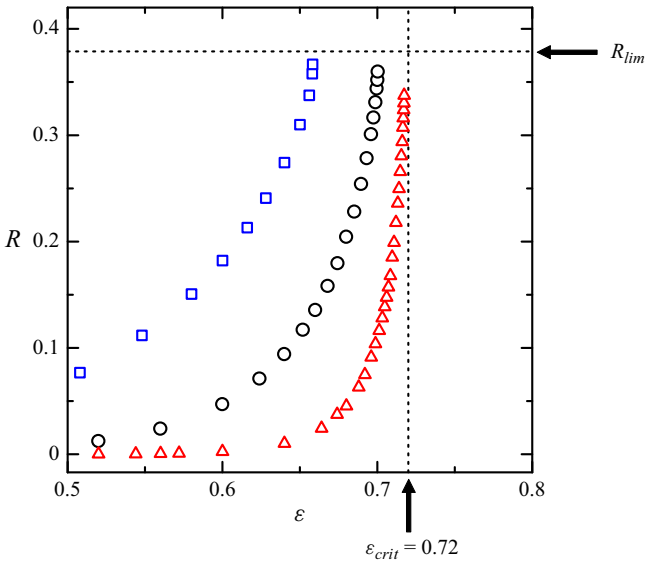


Figure 6. Numerically computed wave amplitude R (defined as half the crest-to-trough height) versus topography peak height ε in the vicinity of $\varepsilon_{crit} = 0.72$: $\mu = 0.05$ (red triangle); 0.1 (black circle); 0.2 (blue rectangle). The horizontal dotted line is an estimate of the limiting amplitude R_{lim} of the Stokes wave.

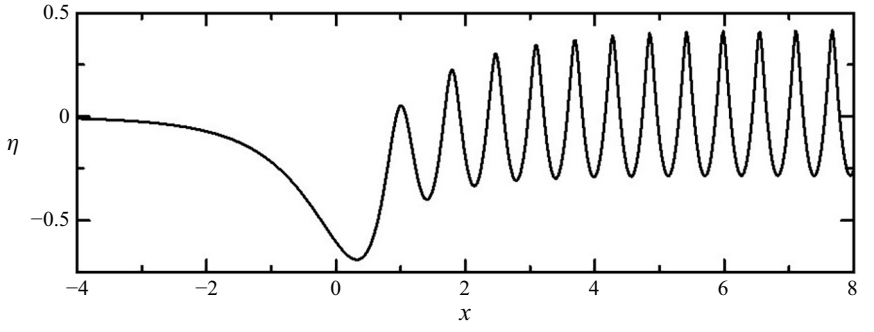


Figure 7. Numerically computed free-surface profile $\eta(x)$ when $\mu = 0.1$ and the topography peak height ε is slightly below $\varepsilon_{lim} = 0.70$ for this μ (figure 6).

the onset of wave breaking. Interestingly, this wave-breaking phenomenon is not associated with the long wave disturbance over the topography predicted by the hydraulic solution for $\mu \ll 1$. Instead, the wave breaking is triggered by the (formally exponentially small with respect to μ) short-scale wave train downstream, which regardless of μ grows sharply and reaches $O(1)$ amplitude as the topography peak height gets close to ε_{lim}.

8. Concluding remarks

This study revisits steady two-dimensional free-surface flow due to a uniform stream flowing over smooth, locally confined bottom topography. Earlier theoretical treatments were based on the nonlinear shallow-water equations, which are derived from the full potential flow equations in the limit of long waves. Thus, on physical grounds, one expects this so-called hydraulic theory to be a valid approximation for flow over topography of large horizontal extent ($\mu \ll 1$) and Froude number $F = O(1)$. Under these conditions

https://doi.org/10.1017/jfm.2026.11312 Published online by Cambridge University Press

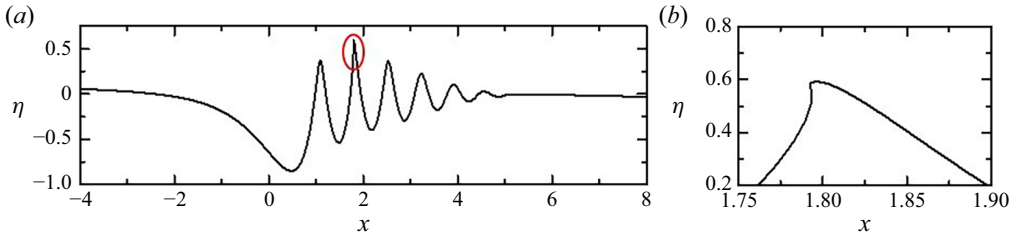


Figure 8. Unsteady free-surface profile $\eta(x, t)$ at $t = 107$, when a downstream wave crest (marked with red circle) first overhangs. Panel (b) zooms in on the overhanging crest. The flow was computed by initiating the uniform stream impulsively at $t = 0$, for $F = 0.5$, $\mu = 0.1$ and topography peak height $\varepsilon = 0.76 > \varepsilon_{lim} = 0.70$.

and subcritical flow ($F < 1$), the hydraulic solution is a steady disturbance confined in the vicinity of the topography if the topography peak height ε is below a certain critical value, $\varepsilon_{crit}(F)$; when $\varepsilon > \varepsilon_{crit}$, the oncoming flow is partially blocked by the topography and hydraulic jumps form upstream and downstream.

The nonlinear shallow-water equations neglect the effects of dispersion altogether. The present analysis focuses on how these effects (controlled by $\mu \ll 1$) may influence the locally confined steady wave disturbance predicted by the hydraulic theory for $F < 1$ and $\varepsilon < \varepsilon_{crit}$. Specifically, based on the dispersion relation of gravity water waves, for $F < 1$, it is possible for a steady radiating wave to appear downstream. However, when $\mu \ll 1$, this wave is much shorter than the topography width, which suggests that (for smooth topography profile whose Fourier transform decays exponentially at large wavenumber) the wave amplitude is exponentially small with respect to μ. Thus, one might expect that this dispersive wave downstream is insignificant relative to the $O(1)$ hydraulic disturbance over the topography.

Contrary to the heuristic argument above, our asymptotic analysis of the full potential flow equations for $\mu \ll 1$ reveals that the short-scale dispersive wave downstream is in fact a prominent part of the wave response, particularly as ε approaches ε_{crit}. While the wave amplitude is indeed exponentially small with respect to μ, $R = O(\exp(-q/\mu))$, the exponent q is controlled by nonlinearity via the topography peak height parameter ε. Specifically, q is a decreasing function of ε and $q \to 0$ as $\varepsilon \to \varepsilon_{crit}$. Thus, increasing the topography peak height amplifies exponentially the radiating wave amplitude, and as ε approaches ε_{crit} this (formally exponentially small) wave reaches the same level as the hydraulic wave disturbance. As a result, the nonlinear shallow-water equations break down in the vicinity of ε_{crit} regardless of $\mu \ll 1$.

The present analysis makes use of exponential asymptotics combined with inner–outer matching. The 'inner' solution is obtained by a multiple-scale expansion in the wavenumber domain, while the 'outer' (far-field) solution accounts for the modulation of the short-scale radiating wave train by the hydraulic disturbance in the physical domain. Upon computing the Fourier transform of the outer solution, the amplitude and phase of the radiating wave are determined by matching these two solutions in an appropriate overlap wavenumber range.

Here, the exponential-asymptotics treatment focuses on a specific class of topography profiles (cf. (2.17)). However, the same procedure applies to any smooth even topography profile $h(x)$ (e.g. a Gaussian) at finite $\varepsilon < \varepsilon_{crit}$ such that the dominant singularities are branch points at $x = \pm i\gamma$ (scenario (i) in § 4). Under this condition (generally satisfied for $\varepsilon = O(1)$ below ε_{crit}), the inner solution (4.25), including the constant C_0 in (4.24), is universal. Furthermore, the far-field solution (5.29) is valid for any smooth even $h(x)$.

https://doi.org/10.1017/jfm.2026.11312 Published online by Cambridge University Press

Thus, the analytical expressions (6.3) for the radiating wave amplitude and phase remain intact (with γ, A and $\tilde{\kappa}(x)$ depending on the specific $h(x)$).

The results of the asymptotic analysis are supported by numerical solutions of the full steady potential flow equations. In particular, these computations confirm that when ε approaches ε_{crit} the radiating wave grows sharply and becomes comparable with the hydraulic disturbance. Furthermore, there is a limiting ε, $\varepsilon_{lim} \approx \varepsilon_{\text{crit}}$, depending on μ and F, such that no steady solution that decays to zero far upstream and remains finite downstream can be computed when $\varepsilon > \varepsilon_{lim}$. For ε just below ε_{lim}, the computed steady wave downstream resembles a steep Stokes periodic wave. In addition, unsteady numerical computations turning on the uniform stream far upstream impulsively, indicate that when ε is slightly above ε_{lim} an oscillatory disturbance forms downstream, which steepens and breaks.

Finally, the present theoretical findings bring out the need for experiments that focus on the wave response downstream. While existing experimental observations (Long 1954, 1970) do not report any downstream waves, our results suggest that such waves play an important part within a range of topography peak heights around ε_{crit}. Specifically, as ε is increased towards and past ε_{crit}, we expect generation of steep waves followed by wave breaking downstream, before upstream influence due to blocking of the flow by the topography eventually sets in.

Declaration of interests. The authors report no conflict of interest.

Data availability statement. The data that support the findings of this study are available on request from T.K.

Appendix A. Derivation of (4.9)

We derive (4.9) from (4.2) expressed in the physical domain. To leading order $O(1)$, (4.2*a*) recovers the hydraulic solution $\widetilde{U} = 1 + u_0$ (cf. (2.9)). Correct to $O(\mu^2)$, the left-hand side of (4.2*a*), with the aid of (4.2*c*), then takes the form

$$(1+u)(D+\eta-\varepsilon h) - D \to \mu^2 \left\{ G(x)u_2 + \frac{\widetilde{U}^3}{2}\eta_{0x}^2 \right\}, \tag{A1}$$

where

$$G(x) = \widetilde{D} - \widetilde{U}^2 \tag{A2}$$

and $\widetilde{D} = D + \eta_0 - \varepsilon h$ is the local depth in the hydraulic solution. Furthermore, the right-hand side of (4.2*a*), with the aid of (4.2*b*), is expressed as

$$\begin{aligned}(w-u)\varepsilon h + \frac{\mu^2}{6}\left\{(1+u)\left((D+\eta)^3 - (\varepsilon h)^3\right)\right\}_{xx} \\ \to \mu^2 D\left(-\frac{1}{2}(D+\eta_0+\varepsilon h)_{xx}\varepsilon h + \frac{1}{6}\left\{\widetilde{D}^2 + 3(D+\eta_0)\varepsilon h\right\}_{xx}\right).\end{aligned} \tag{A3}$$

Therefore, combining (A1) and (A3), u_2 satisfies

$$G(x)u_2 = \frac{D}{6}\frac{\mathrm{d}^2\widetilde{D}^2}{\mathrm{d}x^2} + r_0(x), \tag{A4}$$

where

$$r_0(x) = -\frac{D}{2}(D+\eta_0+\varepsilon h)_{xx}\,\varepsilon h + \frac{D}{2}\{(D+\eta_0)\varepsilon h\}_{xx} - \frac{\widetilde{U}^3}{2}\eta_{0x}^2. \tag{A5}$$

https://doi.org/10.1017/jfm.2026.11312 Published online by Cambridge University Press

Finally, evaluating (A4) close to the singularities $x \to \pm \mathrm{i}\gamma$ using (4.5) and (4.7),

$$G(x) \sim 3D^{1/3}A\sqrt{\gamma \pm \mathrm{i}x}, \quad \frac{\mathrm{d}^2\widetilde{D}^2}{\mathrm{d}x^2} \sim \frac{DA}{2(\gamma \pm \mathrm{i}x)^{3/2}}, \quad r_0(x) \sim O\big((\gamma \pm \mathrm{i}x)^{-1}\big) \ \ (x \to \pm \mathrm{i}\gamma), \tag{A6}$$

by dominant balance we obtain (4.9) for u_2. Furthermore, using (4.2*b*, *c*), we deduce (4.9) for w_2 and η_2.

Appendix B. Derivation of amplitude equation (4.18)

We derive the amplitude equation (4.18) by substituting (4.15) along with (4.16) in (4.2). To this end, with the aid of (4.2*c*) and (2.9), the left-hand side of (4.2*a*) becomes

$$\mathbb{F}\,[M(x) - D] = \mathbb{F}\left[G(x)u_s - \frac{3\widetilde{U}}{2}u_s^2 - \frac{u_s^3}{2} + \mu^2\frac{(1+u)^3}{2}\eta_x^2\right], \tag{B1}$$

where

$$M(x) = (1+u)(D+\eta-\varepsilon h), \tag{B2}$$

and $G(x)$ is defined by (A2). Next, using a similar procedure to that leading to (A3), the right-hand side of (4.2*a*) becomes

$$\begin{aligned}&\mathbb{F}[(w-u)\varepsilon h] - \frac{\mu^2k^2}{6}\mathbb{F}\left[(1+u)\left((D+\eta)^3 - (\varepsilon h)^3\right)\right]\\ &= \mu^2\mathbb{F}\left[-\frac{1}{2}\{M(x)(D+\eta+\varepsilon h)\}_{xx}\,\varepsilon h + \frac{1}{6}\left\{M(x)\left((D+\eta-\varepsilon h)^2 + 3(D+\eta)\varepsilon h\right)\right\}_{xx}\right],\end{aligned} \tag{B3}$$

where we used (4.2*b*) and (2.9). Combining (B1) and (B3), yields

$$\mathbb{F}\left[G(x)u_s - \frac{3\widetilde{U}}{2}u_s^2 - \frac{u_s^3}{2}\right] = \mu^2\mathbb{F}\left[\frac{1}{6}\left\{M(x)(D+\eta-\varepsilon h)^2\right\}_{xx} + r(x)\right] + O\big(\mu^4k^4\hat{u}\big), \tag{B4}$$

where

$$r(x) = -\frac{1}{2}\{M(x)(D+\eta+\varepsilon h)\}_{xx}\,\varepsilon h + \frac{1}{2}\{M(x)(D+\eta)\varepsilon h\}_{xx} - \frac{(1+u)^3}{2}\eta_x^2. \tag{B5}$$

Now, based on (B4), we derive the amplitude equation (4.18) for $\hat{U}_s(K)$ with $K = O(1) > 0$. According to the straightforward expansion (4.1) and the two-scale expansion (4.16),

$$\hat{u}_s(k;\,\mu) \sim \begin{cases} O(\mu^2) & (|k| \lesssim 1/\delta) \\ \mu^{6/5}\hat{U}_s(K)\mathrm{e}^{-\gamma|k|} & (|k| \gtrsim 1/\delta), \end{cases} \tag{B6}$$

where $\mu^{4/5} \ll \delta \ll 1$ (cf. (4.13)). Also, according to (A6), $\hat{G}(k)$ behaves like

$$\hat{G}(k) \sim \begin{cases} O(1) & (|k| \lesssim 1/\delta) \\ \left(-\dfrac{3D^{1/3}A}{2\sqrt{\pi}|k|^{3/2}} + \cdots\right)\mathrm{e}^{-\gamma|k|} & (|k| \gtrsim 1/\delta). \end{cases} \tag{B7}$$

Then, $\mathbb{F}[G(x)u_s]$ on the left-hand side of (B4) for $K = O(1) > 0$ ($k = O(\mu^{-4/5})$) is evaluated as

https://doi.org/10.1017/jfm.2026.11312 Published online by Cambridge University Press

$$\mathbb{F}[G(x)u_s] \equiv \int_{-\infty}^{\infty} \hat{G}(l)\hat{u}_s(k-l)\mathrm{d}l$$
$$\sim \mu^{8/5}\mathrm{e}^{-\gamma k}\left\{\mu^{-2/5}\int_{-\infty}^{1/\delta} \hat{G}(l)\mathrm{e}^{\gamma l}\hat{U}_s(K-\mu^{4/5}l)\mathrm{d}l\right.$$
$$\left.+\int_{\mu^{4/5}/\delta}^{K-\mu^{4/5}/\delta}\left(-\frac{3D^{1/3}A}{2\sqrt{\pi}\lambda^{3/2}}+\cdots\right)\hat{U}_s(K-\lambda)\mathrm{d}\lambda+O\left(\mu^{8/5}\right)\right\}. \tag{B8}$$

Integrating by parts the integral on the far right-hand side of (B8) and using $\int_{-\infty}^{\infty}\hat{G}(l)\mathrm{e}^{\gamma l}\mathrm{d}l = G(-\mathrm{i}\gamma) = 0$ (see (A6)), we have

$$\mathbb{F}[G(x)u_s] \sim \mu^{8/5}\mathrm{e}^{-\gamma k}\frac{3D^{1/3}A}{\sqrt{\pi}}\int_0^K \lambda^{-1/2}\frac{\mathrm{d}\hat{U}_s(K-\lambda)}{\mathrm{d}K}\mathrm{d}\lambda. \tag{B9}$$

Next, by a similar procedure, the second term $\mathbb{F}[-(3\widetilde{U}/2)u_s^2]$ on the left-hand side of (B4) for $K = O(1) > 0$ is evaluated as

$$\mathbb{F}\left[-\frac{3}{2}\widetilde{U}u_s^2\right] \sim -\frac{3}{2}\mu^{8/5}\mathrm{e}^{-\gamma k}D^{1/3}\int_0^K \hat{U}_s(\lambda)\hat{U}_s(K-\lambda)\mathrm{d}\lambda, \tag{B10}$$

where (B6) and $\widetilde{U} \sim D^{1/3}$ $(x \to \pm\mathrm{i}\gamma)$ (see (4.5*b*)) are used. The last term $\mathbb{F}[-u_s^3/2]$ on the left-hand side of (B4) is subdominant relative to (B9) and (B10).

Regarding the right-hand side of (B4), near the singularity $x \to -\mathrm{i}\gamma$,

$$\frac{1}{6}\left\{M(x)(D+\eta-\varepsilon h)^2\right\}_{xx} \sim \frac{D^2A}{12(\gamma-\mathrm{i}x)^{3/2}}+\frac{D^{5/3}}{3}\frac{\mathrm{d}^2\eta_s}{\mathrm{d}x^2} \quad (x\to-\mathrm{i}\gamma), \tag{B11a}$$
$$r(x) \sim O\left((\gamma-\mathrm{i}x)^{-1}\right)+O\left((\sqrt{\gamma-\mathrm{i}x}\,\eta_s)_{xx}\right) \quad (x\to-\mathrm{i}\gamma), \tag{B11b}$$

where (4.5), (4.7) and $M(x) \sim D + O(\sqrt{\gamma-\mathrm{i}x}\,\eta_s)$ $(x \to -\mathrm{i}\gamma)$ are used. Thus, $r(x)$ in (B11*b*) is subdominant in comparison with (B11*a*). Accordingly, making also use of (4.19), the right-hand side of (B4) for $K = O(1) > 0$ $(k = O(\mu^{-4/5}))$ is evaluated as

$$\mu^2\mathbb{F}\left[\frac{1}{6}\left\{M(x)(D+\eta-\varepsilon h)^2\right\}_{xx}+r(x)\right] \sim \mu^{8/5}\mathrm{e}^{-\gamma k}\left(\frac{D^2A}{6\sqrt{\pi}}K^{1/2}+\frac{D^2}{3}K^2\hat{U}_s(K)\right). \tag{B12}$$

Substituting (B9), (B10) and (B12) into (B4), yields (4.18).

Appendix C. Derivation of (5.29)

We derive (5.29) by evaluating the integral (5.27) asymptotically under condition (5.28). To this end, we focus on the behaviour of the integrand in the neighbourhood of the branch point at $x = -\mathrm{i}\gamma$. Specifically, with $x = -\mathrm{i}\gamma + \mathrm{i}s$, the exponent in (5.27) reads

$$-\gamma k - \frac{\mathrm{i}}{\mu}\int_{-\mathrm{i}\gamma}^{0}\tilde{\kappa}(x')\mathrm{d}x' + \Delta, \tag{C1}$$

where

$$\Delta = \frac{\kappa}{\mu}s - \frac{1}{\mu}\int_0^s \tilde{\kappa}(-\mathrm{i}\gamma+\mathrm{i}s')\mathrm{d}s'. \tag{C2}$$

https://doi.org/10.1017/jfm.2026.11312 Published online by Cambridge University Press

For $s \ll 1$, in view of (5.13) with (4.7), $\tilde{\kappa}(-\mathrm{i}\gamma + \mathrm{i}s') \sim 3D^{-5/6}\sqrt{A}\, s'^{1/4}$, so that

$$\Delta \sim \frac{\kappa}{\mu} s - \frac{12}{5\mu D^{5/6}} \sqrt{A}\, s^{5/4}. \tag{C3}$$

Then, setting $s = (D^{10/3}\kappa^4/3^4A^2)\, y$, it follows that

$$\sqrt{\frac{\Omega(\kappa_0 D)}{\Omega(\tilde{\kappa}\widetilde{D})}}\, \mathrm{e}^{\Delta} \sim J \left(\frac{D^{10/3}\kappa^4}{3^4A^2}\, y \right)^{-3/8} \exp\left\{ \frac{D^{10/3}}{3^4A^2} \frac{\kappa^5}{\mu} \left(y - \frac{4}{5} y^{5/4} \right) \right\}, \tag{C4}$$

where we used $\Omega(\tilde{\kappa}\widetilde{D}) \sim 18A^{3/2}s^{3/4}/D^{1/2}$ ($s \ll 1$) from (4.7) and (5.20), and

$$J = \frac{\sqrt{\Omega(\kappa_0 D)}\, D^{1/4}}{3\sqrt{2}\, A^{3/4}} \tag{C5}$$

is a real constant. The exponent in (C4) has a maximum at $y = 1$ and $\kappa^5/\mu \gg 1$ according to (5.28). Thus, we may use Laplace's method to approximate the integral in (5.27) with the exponential factor (C4), which leads to (5.29).

References

Ablowitz, M.J., Fokas, A.S. & Musslimani, Z.H. 2006 On a new non-local formulation of water waves. *J. Fluid Mech.* **562**, 313–343.

Akylas, T.R. 1984 On the excitation of long nonlinear water waves by a moving pressure distribution. *J. Fluid Mech.* **141**, 455–466.

Akylas, T.R. & Yang, T.-S. 1995 On short-scale oscillatory tails of long-wave disturbances. *Stud. Appl. Maths* **94**, 1–20.

Baines, P.G. 1995 *Topographic Effects in Stratified Flows*. Cambridge University Press.

Belward, S.R. & Forbes, L.K. 1993 Fully non-linear two-layer flow over arbitrary topography. *J. Engng Maths* **27**, 419–432.

Cole, S.L. 1985 Transient waves produced by flow past a bump. *Wave Motion* **7**, 579–587.

Dold, J.W. & Peregrine, D.H. 1986 An efficient boundary-integral method for steep unsteady water waves. In *Numerical Methods for Fluid Dynamics II* (ed. K.W. Morton & M.J. Baines), pp. 671–679. Oxford University Press.

Houghton, D.D. & Kasahara, A. 1968 Nonlinear shallow fluid flow over an isolated ridge. *Commun. Pure Appl. Maths* **21**, 1–23.

Kataoka, T. & Akylas, T.R. 2022 Nonlinear effects in steady radiating waves: an exponential asymptotics approach. *Physica D* **435**, 133272.

Kataoka, T. & Akylas, T.R. 2024 Steady radiating gravity waves: an exponential asymptotics approach. *Water Waves* **6**, 79–96.

Kataoka, T. & Akylas, T.R. 2025 Exponential-asymptotics treatment of steady radiating waves from sources of finite strength. *Physica D* **481**, 134832.

Liapidevskii, V.Yu & Gavrilova, K.N. 2008 Dispersion and blockage effects in the flow over a sill. *J. Appl. Mech. Tech. Phys.* **49**, 34–45.

Long, R.R. 1954 Some aspects of the flow of stratified fluids II. Experiments with a two-fluid system. *Tellus* **6**, 97–115.

Long, R.R. 1970 Blocking effects in flow over obstacles. *Tellus* **22**, 471–480.

Lustri, C.J., McCue, S.W. & Binder, B.J. 2012 Free surface flow past topography: a beyond-all-orders approach. *Eur. J. Appl. Maths* **23**, 441–467.

Stoker, J.J. 1957 *Water Waves: The Mathematical Theory with Applications*. Wiley Interscience.

Trinh, P.H. & Chapman, S.G. 2015 Exponential asymptotics with coalescing singularities. *Nonlinearity* **28**, 1229–1256.

Whitham, G.B. 1974 *Linear and Nonlinear Waves*. Wiley Interscience.

Williams, J.M. 1981 Limiting gravity waves in water of finite depth. *Phil. Trans. R. Soc. Lond. A* **302**, 139–188.

https://doi.org/10.1017/jfm.2026.11312 Published online by Cambridge University Press